Magnetocontrollable droplet mobility on liquid crystal-infused porous surfaces

Yang Xu[1], Yuxing Yao[2], Weichen Deng[1], Jen-Chun Fang[1], Robert L. Dupont[1], Meng Zhang[1], Simon Čopar[3], Uroš Tkalec[4,5,6], and Xiaoguang Wang[1,7] (✉)

[1] *William G. Lowrie Department of Chemical and Biomolecular Engineering, The Ohio State University, Columbus, OH 43210, USA*

[2] *Division of Chemistry and Chemical Engineering, California Institute of Technology, Pasadena, CA 91125, USA*

[3] *Department of Physics, Faculty of Mathematics and Physics, University of Ljubljana, 1000 Ljubljana, Slovenia*

[4] *Institute of Biophysics, Faculty of Medicine, University of Ljubljana, 1000 Ljubljana, Slovenia*

[5] *Department of Physics, Faculty of Natural Sciences and Mathematics, University of Maribor, 2000 Maribor, Slovenia*

[6] *Department of Condensed Matter Physics, Jožef Stefan Institute, 1000 Ljubljana, Slovenia*

[7] *Sustainability Institute, The Ohio State University, Columbus, OH 43210, USA*

ABSTRACT

Magnetocontrollable droplet mobility on surfaces of both solids and simple fluids have been widely used in a wide range of applications. However, little is understood about the effect of the magnetic field on the wettability and mobility of droplets on structured fluids. Here, we report the manipulation of the dynamic behaviors of water droplets on a film of thermotropic liquid crystals (LCs). We find that the static wetting behavior and static friction of water droplets on a 4'-octyl-4-biphenylcarbonitrile (8CB) film strongly depend on the LC mesophases, and that a magnetic field caused no measurable change to these properties. However, we find that the droplet dynamics can be affected by a magnetic field as it slides on a nematic 8CB film, but not on isotropic 8CB, and is dependent on both the direction and strength of the magnetic field. By measuring the dynamic friction of a droplet sliding on a nematic 8CB film, we find that a magnetic field alters the internal orientational ordering of the 8CB which in turn affects its viscosity. We support this interpretation with a scaling argument using the LC magnetic coherence length that includes (i) the elastic energy from the long-range orientational ordering of 8CB and (ii) the free energy from the interaction between 8CB and a magnetic field. Overall, these results advance our understanding of droplet mobility on LC films and enable new designs for responsive surfaces that can manipulate the mobility of water droplets.

KEYWORDS

liquid crystals, lubricated surfaces, magnetic field, wettability, droplet mobility

1 Introduction

The manipulation of water droplet mobility on surfaces is critical for a wide range of applications, such as water harvesting [1–5], open-surface microfluidics [6–12], medical diagnostics [13–16], and drug delivery [17–20]. In nature, the hydrophobicity and topography of biological surfaces have been widely utilized to tune the wetting behavior and mobility of water droplets on surfaces, such as directional water droplet transport on spider silks [21], Namib desert beetles [22], and cactus spines [23]. Inspired by these findings, a variety of external fields, including electric [24–26], acoustic [27, 28], and optical [15, 29, 30], have been utilized to change the hydrophobicity and topography of surfaces to tune water droplet mobility. Among the above-mentioned external stimuli, magnetic fields have attracted attention because of their advantages in being easily and remotely controllable [18, 31–35]. Past studies have shown that magnetic colloidal particles that are added to a water droplet can enable the droplet to be pulled across a hydrophobic surface using an applied magnetic field [18, 36]. In addition to the magnetic particle-induced droplet movement, the surface roughness of magnetic fluid/nanostructured surfaces can be manipulated using a gradient magnetic field which then creates a Laplace pressure gradient-triggered directional transport of water droplets [37–39]. Recently, Aizenberg et al. reported the design of ferrofluid-containing liquid-infused porous surfaces, in which various interfacial topographical reconfigurations at multiple length scales can be achieved to regulate the transport of water droplets across their surface [37]. To date, current magnetic-responsive surfaces rely on dispersed magnetic colloidal particles within isotropic solids or simple fluids (e.g., water). The possibility of using structured fluids, whose constituent molecular order can respond to external magnetic fields, to manipulate water droplet transport has not been explored.

As a representative structured fluid, the constituent molecules (mesogens) of liquid crystals (LCs) adopt a rich palette of positional order (i.e., the 3-dimensional organization common in solids) and orientational order (i.e., all molecules pointing in the same direction), and have been shown to respond to a wide range of external stimuli including thermal, optical, electric, and

magnetic fields [40–48]. Recently, our group has developed a class of liquid crystal-infused porous surfaces (LCIPS) that are stable against water-induced dewetting and has demonstrated that the mobility of water droplets on these surfaces can be tuned using heat and ultraviolet (UV) light [49, 50]. In this work, we report the effect of a magnetic field on the behaviors of water droplets on LCIPS. Specifically, we found that the magnetic field causes no measurable change to the apparent contact angle and static friction of water droplets on the LCIPS. In addition, we observed that while in the nematic phase, where the constituent molecules have a long-range orientational order but no positional order (Fig. 1(a)), the applied magnetic field can alter the orientational ordering of the LC, changing the effective viscosity of the LCs surrounding the water droplet, and thus affecting the dynamic friction and the associated water droplet sliding velocity on the LCIPS. In contrast, in both the smectic A phase (where the constituent molecules have both long-range orientational order and positional order) and the isotropic phase (where there is no intrinsic order) (Fig. 1(a)), the magnetic field causes no measurable change to the water droplet mobility on the LCIPS. Overall, our results reveal that the intrinsic LC molecular ordering can be selectively tuned to influence the mobility of water droplets under an applied magnetic field, which provides an entirely new route for the manipulation of water droplet transport across structured fluid surfaces.

2　Experimental section

2.1　Materials

4'-Octyl-4-biphenylcarbonitrile (8CB), 4-cyano-4'-pentylbiphenyl (5CB), E7 (a blend of 51% 5CB, 25% 4-cyano-4'-n-heptyl-biphenyl, 16% 4-cyano-4'-n-oxyoctyl-biphenyl, and 8% 4-cyano-4'-n-pentyl-terphenyl), and reactive LC 1,4-bis-(4-(3-acryloyloxypropyloxy)benzoyloxy)-2-methylbenzene (RM257) were purchased from Jiangsu Hecheng Advanced Materials Co., Ltd. Photoinitiator 2,2-dimethoxy-2-phenylacetophenone (DMPAP) and dimethyloctadecyl(3-(trimethixysilyl) propyl) ammonium chloride (DMOAP, 42 wt.% in methanol) were purchased from Sigma-Aldrich. 190 proof ethanol was purchased from Decon Labs Inc. Plain microscope slides were purchased from Fisher Scientific. The magnet using in this work was purchased from K&J Magnetics, Inc. The water used in all of the experiments was purified using a Milli-Q water purification system (Simplicity C9210). Unless stated otherwise, the purchased chemicals were used as received without further modification or purification.

2.2　Preparation of DMOAP-functionalized glass slides

Microscope slides were cleaned with water and ethanol and then dried under a stream of nitrogen gas. Next, the cleaned microscope slides were soaked in a 1% v/v DMOAP water solution for 15 min. Then, the microscope slides were taken out from the solution and cleaned with water and ethanol to remove residual unreacted DMOAP. After drying under a stream of nitrogen gas, the obtained slides were stored in an aluminum-covered container to prevent light from affecting the DMOAP layer.

2.3　Preparation of LCIPS

First, we prepared a reactive LC mixture composed of 8CB (90 wt.%) and RM257 (10 wt.%). A photoinitiator, DMPAP, was added at 1 wt.% based on the LC mixture. Then, 100 μL of the LC mixture was spread evenly on a DMOAP treated glass slide (2.5 cm × 2.5 cm). Afterward, two ~ 160 μm spacers were placed

on either edge of the DMOAP treated glass slide and a second DMOAP treated glass slide was placed on top. Subsequently, the construction was exposed to 2.0 mW/cm² UV light (Spectroline, EA-140; 365 nm) for 20 min at 35 °C to polymerize the 8CB swollen porous polyRM257 substrate. Finally, we removed the top DMOAP-functionalized glass slide and drop-cast excess 8CB (80 μL) onto the polyRM257 porous structure to make an 8CB-infused porous polyRM257 surface (8CB-based LCIPS) with a 130 μm-thick lubricating 8CB layer, which prevents water placed on top from directly contacting the polyRM257 porous structure. The 5CB and E7-infused surfaces were obtained in a similar method as that of 8CB-infused surfaces. Unless stated otherwise, 8CB was used in the LCIPS throughout this research.

2.4　Characterization of the morphology of porous polyRM257 substrates

The porous polyRM257 substrate used for the scanning electron microscopy (SEM) imaging was prepared from the photopolymerization of a mixture of 10 wt.% RM257 in 8CB followed by an extraction of the nonreactive 8CB with ethanol. After being fully dried, the porous substrate was coated with a thin layer of gold before imaging. Finally, the morphology of the porous polyRM257 substrate was imaged using an FEI Quanta 200 SEM with an acceleration voltage of 5 kV at a working distance of ~ 9 mm (Fig. S1 in the Electronic Supplementary Material (ESM)).

2.5　Characterization of the orientational ordering of the LCIPS

The orientational ordering of the LCIPS in air was characterized using an Olympus BX53 microscope equipped with crossed polarizers. We controlled the temperature of the LCIPS using a Linkam PE120 Peltier hot stage to investigate the different phases. We dropped a 1 μL droplet of pure water on the LCIPS in the smectic A (25 °C) and nematic (35 °C) phases to show the optical image under different phases.

2.6　Characterization of the wetting of water droplets on LCIPS

The apparent contact angles and hysteresis of water droplets on LCIPS were measured using a KRÜSS DSA 100 contact angle goniometer. To minimize the dynamic force acting on the droplet which could cause the shape to deform, we pushed the plunger in the syringe slowly (5 μL/min) during these measurements to make the 3 μL water droplets. We used a Linkam PE120 Peltier hot stage to control the temperature of the LCIPS to achieve the different phases. Each data point was measured at least three times for each condition. The contact angle hysteresis is defined as $\cos\theta_{rec} - \cos\theta_{adv}$.

2.7　Characterization of the mobility of water droplets on LCIPS

The sliding angle of a water droplet on an LCIPS was measured with a goniometer. Typically, a 3 μL water droplet was placed on the LCIPS, and the KRÜSS ADVANCED software was used to tilt the surface with a rate of 1 °/min. The sliding angle is defined as the angle where the droplet started to move. For the velocity measurements, an LCIPS was placed on a pre-tilted 7° platform while in the isotropic and nematic phase. We dropped a 3 μL water droplet on the top of the surface, close enough to the surface to prevent any initial velocity. Then the pure water droplet was allowed to slide across 2 cm of the surface. The time needed to cross this distance was used to calculate the average velocity. We

used the Tracker open-source software to analyze the videos to calculate the velocity. A magnetic field was applied by placing a magnet close to the LCIPS with the direction of the magnetic field being tuned by changing the location and orientation of the magnet with respect to the LCIPS. For different magnetic field intensities, we changed the distance between the LCIPS surface and the magnet, based on a magnet calculator on the K&J Magnetics, Inc website [51].

2.8 Measuring the friction force of water droplets on LCIPS

A cantilever, made of an arylate needle with a 300 μm inner diameter and a 700 μm outer diameter, was employed as a force sensor, which could sense a dissipative force (F_d) as small as 0.1 μN. We fixed the top end of the cantilever on the goniometer and the bottom end to a pure water droplet, which was placed on the top of the substrate that was sitting on a ThorLabs PRM1Z8 rotation stage. The angular velocity of the rotation stage was set between 0.1 and 0.5 °/s. The droplet was placed 1–2 cm away from the center of rotation. After the stage rotated, the bottom end of the needle began to bend (the corresponding needle displacement was Δx), which was recorded by the camera on the goniometer and measured with the open-source software, Tracker. The deformation Δx followed Hooke's law

$$F_d = k\Delta x \tag{1}$$

where k = 17.3 mN/m is the elastic constant of the acrylate needle, which was determined in advance by putting different weights of the pure water droplets on the end of the needle as it was held horizontally. A magnetic field was applied by placing a magnet close to the LCIPS with the direction of the magnetic field being tuned by changing the location and orientation of the magnet with respect to the LCIPS.

3 Results and discussion

The LCIPS were prepared by infusing LCs into a porous LC polymeric network, as shown in Fig. 1(b). We selected 8CB as the LC in this study because it exhibits LC mesophases with different molecular orders [40], as summarized in Fig. 1(a). When a water droplet was placed on an LCIPS in the nematic phase, the 8CB in contact with air was dark and the 8CB in contact with the droplet was bright, when viewed under a polarized light microscope, as shown in Figs. 1(c) and 1(d). This is consistent with the surface anchorings of nematic 8CB at the air–8CB interface (perpendicular to the interface) and water–8CB interface (parallel to the interface) [47]. When a water droplet was placed on an LCIPS in the smectic A phase, focal conic domain arrays were formed at the smectic A 8CB–water interface, which is consistent with the parallel anchoring at the water–8CB interface [52–55], as shown in Figs. 1(e) and 1(f). These results demonstrate that the porous polyRM257 network can stabilize 8CB against dewetting by water droplets, which is consistent with our past studies (see details in the ESM) [49, 50, 56].

In the first set of experiments, we investigated the effect of the magnetic field on the wetting behavior of water droplets on an LCIPS. As shown in Fig. 2(a), the apparent advancing contact angles of a water droplet on an LCIPS remained almost constant over the smectic A, nematic, and isotropic phases. Upon applying an external magnetic field (~ 0.56 T) perpendicular to the LCIPS (placing a magnet on the bottom of the LCIPS), no measurable changes to the apparent advancing contact angles of the water droplets on the LCIPS were observed over all LC mesophases (Fig. 2(b)). In addition, we observed no significant changes to the shape of sessile water droplets (e.g., wetting ridges and contact angles) on
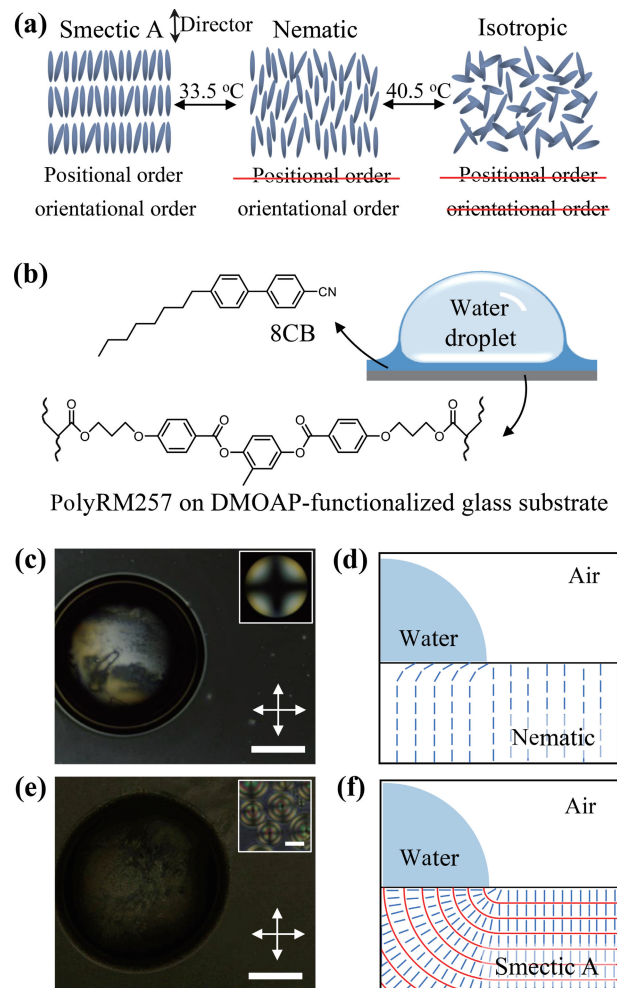
Figure 1 (a) Temperature-dependent phase behaviors of 8CB. (b) Schematic illustration of a water droplet on an LCIPS and the structure of the 8CB mesogen and LC polymer. (c) and (e) Polarized light micrograph (top view) of a 1 μL water droplet on an 8CB film in the (c) nematic and (e) smectic A phase, respectively. The crossed double-headed arrows indicate the orientations of the crossed polarizers. Scale bars, 500 μm. Inset in (c) is a conoscopic image confirming the homeotropic alignment of 8CB at the interface of air–8CB surface and the interface between the 8CB and polyRM257-coated substrate. Inset in (e) shows a corresponding high magnification image of the focal conic domain structure of smectic A 8CB under a water droplet, suggesting a planar alignment of smectic A 8CB at the water–8CB interface and a homeotropic alignment at the 8CB–polyRM257-coated substrate. The scale bar in the inset of (e) is 20 μm. (d) and (f) Schematic illustration of the orientational ordering of an 8CB film in the (d) nematic and (f) smectic A phase with a water droplet on its surface. The blue lines represent the individual 8CB mesogens and the red lines represent the lamellar structure in the smectic A 8CB. The schemes are not drawn to scale.

the LCIPS before and after applying the external magnetic field. It should be noted that the contact angle of water droplets on LCIPS depends on the intermolecular interactions (van der Waals force) between the LCs and water. These short-range intermolecular interactions result in a surface-induced planar anchoring of the LCs under the water droplets, which is independent of the magnetic field. As a result, the magnetic field has no influence on the contact angle and contact angle hysteresis of water droplets on an LCIPS. These observations lead us to conclude that the magnetic field has no effect on the wettability of water droplets on LCIPS.

Next, we sought to explore the effect of a magnetic field on the mobility of water droplets on the LCIPS. Water droplets start sliding across tilted solid or liquid surfaces only when the dynamic component of gravitational force ($F_{gravitation} \sin\alpha$) acting on the
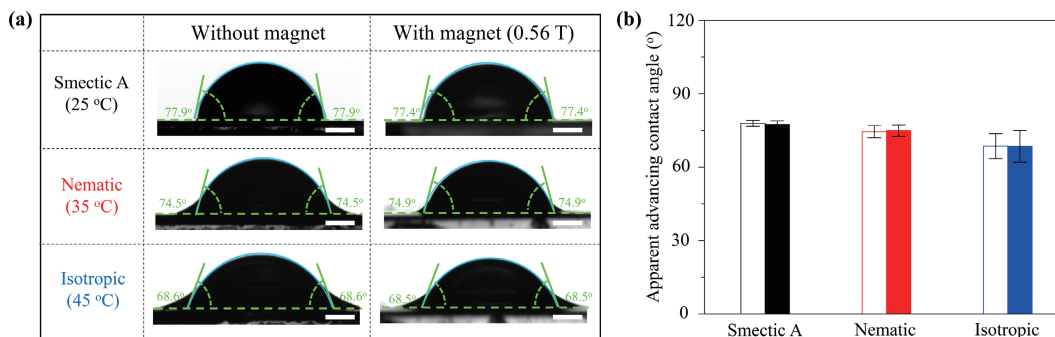
Figure 2 (a) Goniometer photographs and (b) the corresponding plot showing the effect of a magnetic field on the apparent advancing contact angles of water droplets on 8CB-based LCIPS in different LC mesophases. The magnetic field was applied perpendicular to the LCIPS. The LCIPS temperature was set at 25 °C, 35 °C, and 45 °C to create the smectic A (black), nematic (red), and isotropic phases (blue), respectively. The filled and open columns represent the apparent contact angles with and without an applied magnetic field, respectively. The volume of each water droplet was 3 µL. Scale bars, 1 mm. Error bars represent standard deviations from three independent measurements for each data point.

water droplet overcomes the lateral static friction force (F_{static}), and the water droplet needs to overcome the subsequent dynamic friction force ($F_{dynamic}$) to maintain their relative motion on the surface [57–65]. To study the effect of the magnetic field on the F_{static} acting on the water droplets sliding on an LCIPS, we measured the sliding angle of the droplets, which is defined as the minimum angle that the surface needs to be tilted to cause the droplets to slide. The static friction can be written as [9, 66, 67]

$$F_{gravitation}\sin\alpha = F_{static} \qquad (2)$$

$$mg\sin\alpha = w(\gamma_{w–LC} + \gamma_{LC})(\cos\theta_R - \cos\theta_A) \qquad (3)$$

where m is the mass of the water droplet, g is the gravitational acceleration, α is the sliding angle of the water droplet on the LCIPS, w is the base diameter of the droplet, $\gamma_{w–LC}$ is the water–LC surface tension, γ_{LC} is the air–LC surface tension, and θ_A and θ_R are the advancing and receding contact angles of the water droplet on the LCIPS, respectively. We comment here that the use of

$(\gamma_{w–LC} + \gamma_{LC})$ instead of the air–water surface tension (γ_w) is due to the formation of a nanometer-thick LC layer around the water droplet (see details in the ESM) [68]. As shown in Fig. 3, the sliding angle and contact angle hysteresis ($\cos\theta_R - \cos\theta_A$) of the water droplets on the LCIPS only depends on the LC mesophases, ~ 35° in the smectic A phase and ~ 3° in the nematic or isotropic phases. We note here that the contact angle hysteresis is calculated using $\cos\theta_R - \cos\theta_A$ due to the difficulty in accurately measuring the θ_A and θ_R of water droplets on lubricated surfaces including LCIPS [62]. The magnetic field was found to cause no measurable change to the sliding angle and thus the static friction of the water droplet on the LCIPS. Our previous studies have reported that the LC mesophase-dependent sliding angle of water droplets is caused by both the LCIPS surface roughness, and the wetting ridge composed of LCs [49]. These results lead us to conclude that the magnetic field has a negligible effect on the LCIPS surface roughness and wetting ridge around the water droplets on an LCIPS.
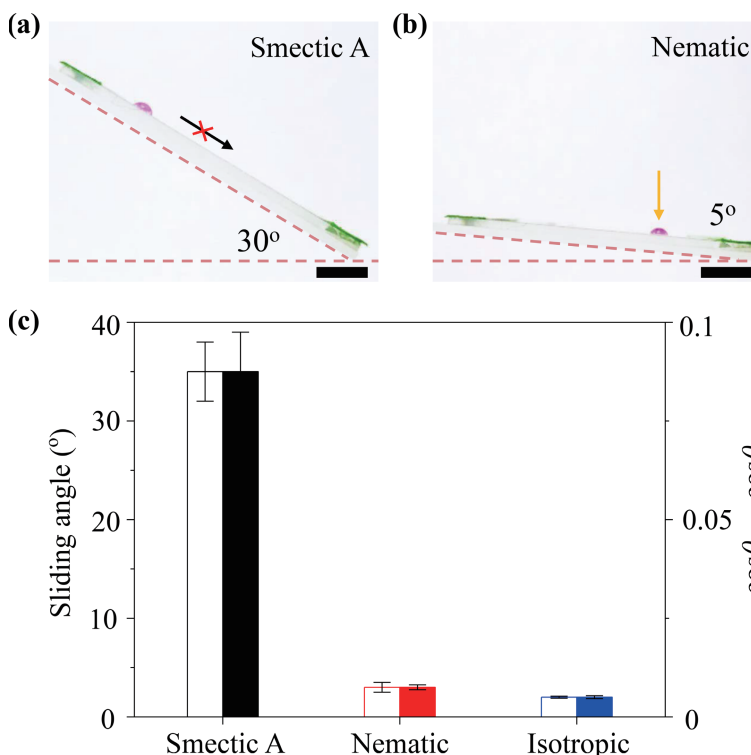
Figure 3 (a) and (b) Photographs and (c) the corresponding plot showing the effect of the magnetic field on the sliding angle (left *y* axis) and contact angle hysteresis (right *y* axis) of water droplets on 8CB-based LCIPS in different LC mesophases. The magnetic field was applied perpendicular to the LCIPS. The LCIPS temperature was set at 25 °C, 35 °C, and 45 °C to reach the smectic A, nematic, and isotropic phases, respectively. The volume of each water droplet was 3 µL and the magnetic field was 0.56 T. Scale bars, 0.5 cm. Error bars represent standard deviations from three independent measurements for each data point.

Furthermore, we investigated the effect of the magnetic field on the $F_{dynamic}$ of a water droplet on an LCIPS. The sliding of a water droplet on a smectic A LCIPS follows a stick-slip mode where the sliding velocity of the water droplet accelerates after overcoming the static friction force ($F_{gravitation}\sin\alpha > F_{dynamic}$) [57]. Considering the fact that the balancing of the gravitational force and hydrodynamic shear of the isotropic liquid (acting as $F_{dynamic}$) results in a constant droplet sliding velocity on an inclined isotropic liquid-infused porous surface ($F_{gravitation}\sin\alpha = F_{dynamic}$), our study of $F_{dynamic}$ only focused on nematic and isotropic LCIPS. In addition, we note that both the apparent advancing and receding contact angles of a moving water droplet is independent of the time taken to slide, which suggests there is no change in the contact area of the droplet sliding on the LCIPS (Fig. S3 in ESM). As shown in Figs. 4(a)–4(c), the sliding velocity of a water droplet on a nematic phase LCIPS in the absence of an applied magnetic field perpendicular to the LCIPS was measured to be ~ 0.85 mm/s. Interestingly, the sliding velocity of the water droplet on a nematic phase LCIPS depends on the relative position of the magnet with respect to the LCIPS. Specifically, when the magnet was placed at the bottom of the LCIPS (the corresponding magnetic field being perpendicular to the LCIPS), the sliding velocity decreased to ~ 0.48 mm/s, whereas placing two magnets next to the LCIPS (the corresponding magnetic field being parallel to the LCIPS) increased the sliding velocity to ~ 1.25 mm/s. The increase (or decrease) in the sliding velocity suggests a decrease (or increase) in the dynamic friction of the water droplet sliding on the LCIPS. We note here that the magnetic field-induced change in the sliding velocity depends on the strength of the magnetic field, as shown in Fig. 4(d). We also note here that the magnetic field-induced change in the sliding velocities of the water droplets was also

observed on LCIPS made of nematic E7 and 5CB (Fig. S4 in the ESM). In contrast, the magnetic field caused no measurable change to the sliding velocities of water droplets on isotropic phase 8CB-based LCIPS and isotropic liquid-infused polyRM257 substrates, such as silicone oil and mineral oil, as shown in Fig. S4 in the ESM. These results lead us to hypothesize that the magnetic field affects the orientational ordering of nematic 8CB, which in turn affects the dynamic friction and sliding velocity of water droplets on nematic LCIPS.

Previous studies have shown that on isotropic liquid-based lubricated surfaces, the $F_{dynamic}$ acting on the moving water droplets is dominated by the viscous dissipation at the rim of the droplet's base [62]. The thickness of the lubricant films underneath the water droplet depends on the sliding velocity rather than any initial conditions (e.g., spin coating parameters), and the $F_{dynamic}$ acting on a moving water droplet increases with an increase in the sliding velocity, which agrees with the Landau–Levich–Derjaguin (LLD) theory [62, 69]. Considering the fact that the classic LLD theory is developed for simple fluids, we fit the apparent viscosity of the LC based on the LLD theory. Accordingly, the $F_{dynamic}$ acting on the moving water droplets on the LCIPS can be written as [62]

$$F_{dynamic} \approx 2\pi\gamma_{w-LC}RCa^{2/3} \qquad (4)$$

in which γ_{w-LC} is the interfacial tension between water and the LC, and R is the base radius of the droplet. Ca is the capillary number, $Ca = \eta U/\gamma_{w-LC}$, where η is the apparent viscosity of the LC and U is the velocity of the moving water droplet. To provide a fundamental insight into the role of the magnetic field, we measured the $F_{dynamic}$ acting on the water droplet on an LCIPS
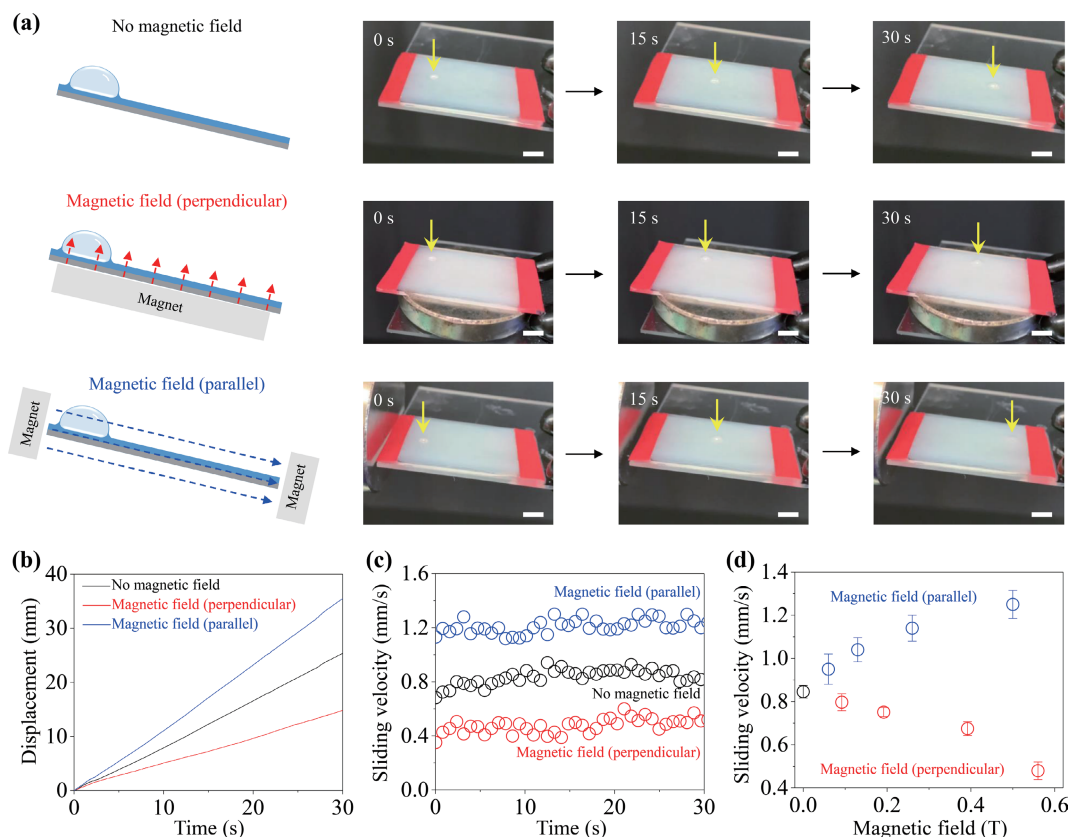
Figure 4 (a) Schematic illustration and corresponding photographs showing the sliding of water droplets on nematic LCIPS with and without magnetic fields in different directions. Scale bars, 1 cm. The volume of the water droplet was 3 μL. (b) Displacement and (c) sliding velocity of water droplets on nematic 8CB films as a function of time with and without a magnetic field. The 8CB film temperature was set at 35 °C to create the nematic phase, and the applied magnetic fields were 0.56 T (perpendicular) and 0.50 T (parallel). (d) Plot showing the sliding velocity as a function of the magnetic field. The black, red, and blue lines or points in (b)–(d) represent the data for trials without a magnet, with a magnetic field that is perpendicular to the LCIPS, and with a magnetic field that is parallel to the LCIPS, respectively. Error bars represent standard deviations from three independent measurements for each data point.
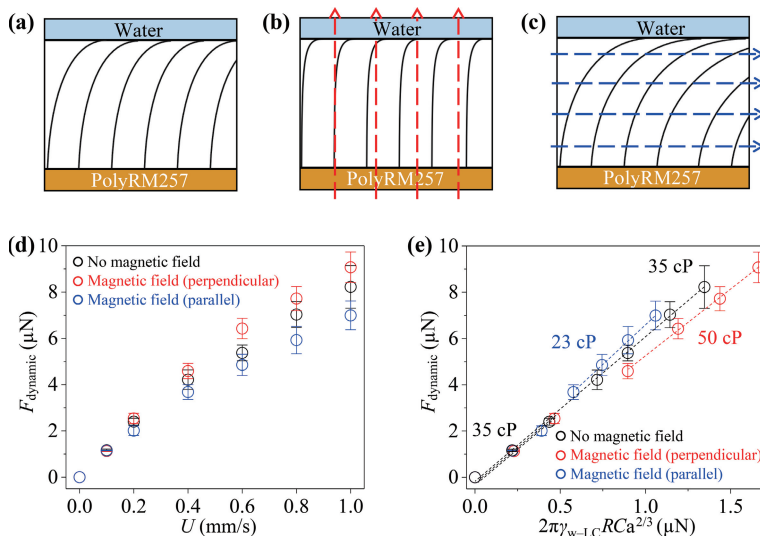
Figure 5 (a)–(c) Schematic illustrations showing the effect of the magnetic field on the LC orientational ordering within the nematic LCIPS. The black lines show the orientation of the mesogens. The red and blue dashed arrows show the magnetic field perpendicular and parallel to the LCIPS, respectively. (d) Plot showing the $F_{dynamic}$ acting on 3 μL water droplets moving at speeds of 0.1–1 mm/s on a nematic 8CB film. The magnetic field strength was 0.56 T for the perpendicular direction and 0.50 T for parallel direction. (e) Plots showing that the $F_{dynamic}$ acting on the 3 μL water droplets on a nematic LCIPS follows the LLD theory predicted by Eq. (3) with and without a magnetic field. The black lines fit the data with η of ~ 35 cP in the absence of a magnetic field and for small velocities in the presence of a magnetic field. The red line fits the data with η of ~ 50 cP for high velocities in the presence of a magnetic field that is perpendicular to the 8CB film. The blue line fits the data with η of ~ 23 cP for high velocities in the presence of a magnetic field that is parallel to the 8CB film. Error bars represent standard deviations from three independent measurements for each data point.

with and without a magnetic field (Figs. 5(a)–5(c)). We note here that the water droplets were slippery on the nematic 8CB films with $F_{static} \approx F_{dynamic}$, which is characteristic of a slippery mode (Fig. S5 in the ESM) [62, 70]. As shown in Fig. 5(d), we observed that the $F_{dynamic}$ increases with an increase in the sliding velocity. The increase in the sliding velocity of the water droplet on the LCIPS causes an increase in the thickness of the 8CB under the water droplet, which in turn increases the viscous dissipation (dynamic friction) that impedes the water droplet sliding [40, 42, 71]. In the absence of a magnetic field, the dynamic viscosity of nematic 8CB was measured to be 35 cP by fitting the $F_{dynamic}$ measurements with $2\pi\ \gamma_{w-LC}\ R\ Ca^{2/3}$ (Fig. 5(e)), which is consistent with previous studies [72]. In the presence of a magnetic field, we measured the dynamic viscosity of the nematic 8CB to be ~ 35 cP for small velocities and ~ 50 cP and ~ 23 cP for high velocities when the magnetic field was applied perpendicular and parallel to the LCIPS, respectively, as shown in Fig. 5(e). In contrast, the dynamic viscosity of isotropic 8CB was measured to be 17 cP, independent of the magnetic field (Fig. S6 in the ESM).

Previous studies have reported that the LC ordering is governed by the LC elasticity, surface anchoring, and external fields [42, 43]. To provide insights into the effect of the magnetic field on the $F_{dynamic}$ acting on the water droplet on an LCIPS, we calculated the magnetic coherence length (ξ) of LCs [73], which describes the thickness above which the director orientation is dominated by the applied magnetic field (below which the director orientation is dominated by the LC elasticity). ξ can be written as [73]

$$\xi = \sqrt{\frac{\mu_0 K}{\Delta\chi B^2}} \quad (5)$$

in which K is the elastic constant, $\Delta\chi$ is the diamagnetic anisotropy, μ_0 is the permeability of vacuum, and B is the strength of the local magnetic field.

By inputting the typical values of the parameters in Eq. (5) (K = 5 pN, $\Delta\chi = 1 \times 10^{-6}$, $\mu_0 = 4\pi \times 10^{-7}$ ((kg·m/s²)/A²), and B = 0.56 T), we estimated ξ to be ~ 4 μm in the presence of a magnetic field with a strength of 0.56 T, which supports our observation of the existence of a threshold velocity above which the magnetic field

has a measurable impact on the $F_{dynamic}$ acting on the water droplets sliding on LCIPS shown in Fig. 5(d). As described earlier, the thickness of the 8CB film under a moving water droplet strongly depends on the sliding velocity of the water droplet. For low sliding velocities which give rise to 8CB films with thickness smaller than ξ, the equilibrium orientational ordering of the nematic 8CB is dominated by the bulk elasticity of 8CB and the magnetic field has a negligible effect. For high sliding velocities which result in nematic 8CB films with thicknesses larger than ξ, the equilibrium 8CB orientational ordering will follow the local applied magnetic field. Because the dynamic viscosity of 8CB that is parallel to the local 8CB director is smaller than that perpendicular to the local 8CB director, the presence of a magnetic field perpendicular (or parallel) to the 8CB film will increase (or decrease) the dynamic viscosity of 8CB around the water droplet and thus the $F_{dynamic}$ acting on the sliding water droplet on an LCIPS. Furthermore, ξ is calculated to decrease from ~ 62 to ~ 4 μm with an increase in the magnetic field strength from 0.04 to 0.56 T (Fig. S7 in the ESM), which supports our observation of magnetic field strength-dependent $F_{dynamic}$ shown in Fig. 4(d). In addition, we observed a bright optical appearance upon applying a horizontal magnetic field to a nematic 8CB film and a dark appearance after removing the magnetic field (Fig. S8 in ESM), suggesting that the magnetic field can reorient the LCs away from the orientation caused by the substrate, which is consistent with past studies of the magnetic coherence length and the Frederick transition of nematic LCs [73]. It should be noted that the applied magnetic field can align the LCs due to their intrinsic anisotropic diamagnetic susceptibility without altering the atomic/molecular structure of the LCs. We note here that we neglected the LC ordering in the LC wrapping layer around the water droplets as its thickness is much smaller than the LC film underneath the droplet. We also comment here that conventional single wavelength reflection interference contrast microscopy, which has been shown to measure the thickness of lubricants underneath water droplets [74], cannot be used for LCs as their refractive indices are not constant.

The above results reveal new principles by which the orientational ordering of an LCIPS and the sliding velocity of

water droplets can be coupled on LCIPS. In the final set of experiments, we sought to use a magnetic field to control the dynamic friction and thus the sliding velocity of water droplets on an LCIPS. As shown in Fig. 6, when the magnetic field was placed under the LCIPS (the corresponding magnetic field was perpendicular to the LCIPS), the water droplets slide at a rate of ~ 0.49 mm/s. After 15 s, the magnet was removed, and the water droplet slid at a rate of ~ 0.8 mm/s. At 30 s, the magnet was placed to the left of the LCIPS (the corresponding magnetic field was parallel to the LCIPS), and the sliding velocity of the water droplets increased to ~ 1.24 mm/s. It should be noted that the time required for the molecular orientational order within the LC film to relax (τ) can be estimated as [47]

$$\tau \sim \frac{\eta h_{\text{film}}^2}{K} \tag{6}$$

where h_{film} is the thickness of the LC film. τ is estimated to be ~ 0.1 s, thus we conclude that the reorganization of LC molecules with respect to the change of the magnetic field is much faster compared with our experimental timescale (tens of seconds). Overall, our experimental observations support our hypothesis that the applied magnetic field changes the orientational ordering of LCs, which affects the F_{dynamic} experienced by moving droplets and thus the sliding velocity of the water droplets on nematic LCIPS.

4 Conclusions

Overall, the results reported in this work advance our understanding of droplet mobility on anisotropic or structured fluids. Our results reveal that an applied magnetic field causes no significant change to the static wetting behaviors (e.g., apparent contact angles) and static friction (e.g., sliding angle) of a water droplet on an 8CB surface in the smectic A, nematic, and isotropic phases. When the droplet is sliding on the 8CB film, however, the magnetic field affects the droplet dynamics in a matter that is dependent on the 8CB mesophase. In the isotropic phase, the droplet velocity is independent of the magnetic field, whereas in the nematic phase, the introduction of a magnetic field can affect the orientational ordering of the LCs and thus changes the sliding velocity of the water droplet. The interplay between the elastic energy and magnetic field contributes to a change in the viscosity of the LCIPS, and thus alters the F_{dynamic} acting on the water droplet on the LCIPS. Giving the broad range of triggers that can perturb the LC orientational ordering, these results provide the basis of a novel methodology for the manipulation of the dynamic friction of a sliding water droplet through tuning the internal structure of the LCs, which may have a range of potential applications, including in chemical sensors and for liquid transport, water harvesting, and open-surface microfluidics. We believe the results reported in this work provide a complementary design strategy to expand the functionality of conventional isotropic liquid-based lubricated surfaces. In future studies, we will investigate other LC mesophases beyond nematic and smectic A, such as the cholesteric phase [40], blue phase [75, 76], and twist-bend nematic phase [77, 78]. Future efforts will seek to study water droplet bouncing on LCIPS, particularly retraction dynamics, which may be largely influenced by the dynamic viscosity of the lubricants coated on the surfaces [79]. In addition,
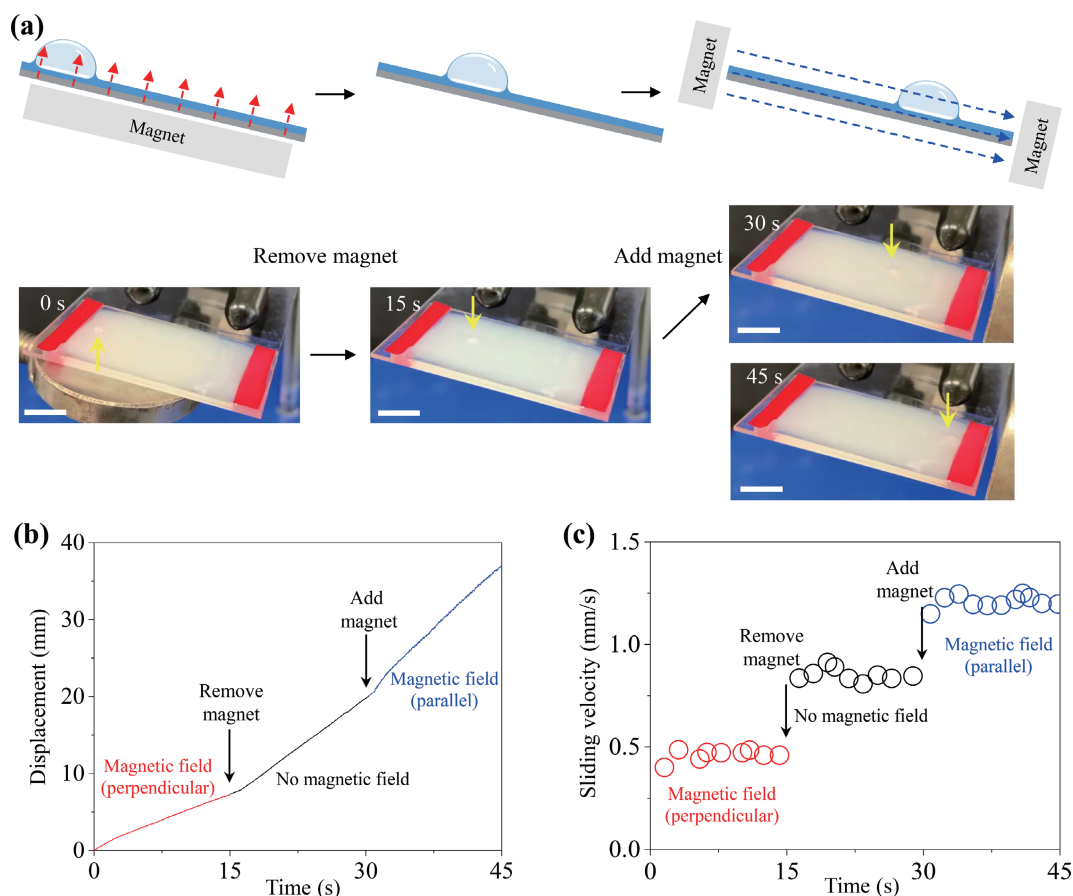
Figure 6 (a) Schematic illustration and photographs showing the programmable movement of a water droplet on a nematic 8CB film through the manipulation of a magnetic field. The corresponding positions of the applied magnetic fields were perpendicular and parallel to the 8CB film. Scale bars, 1 cm. Corresponding plots showing (b) the displacement and (c) the sliding velocity of a water droplet as a function of time. The applied magnetic field strength was 0.56 T for the perpendicular direction and 0.50 T for the parallel direction, and the volume of the water droplet was 3 μL. The black, red, and blue lines or points in (b) and (c) represent the data for trials without a magnet, with a magnetic field that is perpendicular to the LCIPS, and with a magnetic field that is parallel to the LCIPS, respectively.

we will also seek to modify the classic LLD theory to understand water droplet sliding on anisotropic fluids.

Acknowledgements

Electronic Supplementary Material: Supplementary material (further details of the stability of LCIPS against water-induced dewetting, the interfacial tension and contact angle measurement using a goniometer, the estimation of the thickness of LC wrapping layer at air–water interface on droplets, SEM measurements, the average sliding velocity of a water droplet on 5CB, E7, silicone oil, and mineral oil films with and without a magnetic field, representative force diagram (F_d versus time) of a 3-µL water droplet moving at a speed of 0.1 mm/s on a nematic 8CB film, $F_{dynamic}$ acting on 3 µL water droplets moving at speeds of 0.1–1 mm/s on an isotropic 8CB film, the calculated magnetic coherence length as a function of the magnitude of the magnetic field applied to the nematic LCIPS, and the apparent advancing and receding contact angles of a moving water droplet on nematic LCIPS as a function of time, and polarized light micrographs (top view) of a nematic 8CB film between two DMOAP-functionalized glass slides before and after applying a horizontal magnetic field) is available in the online version of this article at https://doi.org/10.1007/s12274-022-5318-y.

References

[1] Xu, W. H.; Zheng, H. X.; Liu, Y.; Zhou, X. F.; Zhang, C.; Song, Y. X.; Deng, X.; Leung, M.; Yang, Z. B.; Xu, R. X. et al. A droplet-based electricity generator with high instantaneous power density. *Nature* **2020**, *578*, 392–396.

[2] Guo, Z. Q.; Zhang, L.; Monga, D.; Stone, H. A.; Dai, X. M. Hydrophilic slippery surface enabled coarsening effect for rapid water harvesting. *Cell Rep. Phys. Sci.* **2021**, *2*, 100387.

[3] Chen, H. W.; Ran, T.; Gan, Y.; Zhou, J. J.; Zhang, Y.; Zhang, L. W.; Zhang, D. Y.; Jiang, L. Ultrafast water harvesting and transport in hierarchical microchannels. *Nat. Mater.* **2018**, *17*, 935–942.

[4] Dai, X. M.; Sun, N.; Nielsen, S. O.; Stogin, B. B.; Wang, J.; Yang, S. K.; Wong, T. S. Hydrophilic directional slippery rough surfaces for water harvesting. *Sci. Adv.* **2018**, *4*, eaaq0919.

[5] Maji, K.; Das, A.; Dhar, M.; Manna, U. Synergistic chemical patterns on a hydrophilic slippery liquid infused porous surface (SLIPS) for water harvesting applications. *J. Mater. Chem. A* **2020**, *8*, 25040–25046.

[6] Shang, L. R.; Cheng, Y.; Zhao, Y. J. Emerging droplet microfluidics. *Chem. Rev.* **2017**, *117*, 7964–8040.

[7] Kaminski, T. S.; Garstecki, P. Controlled droplet microfluidic systems for multistep chemical and biological assays. *Chem. Soc. Rev.* **2017**, *46*, 6210–6226.

[8] Jiang, J. K.; Gao, J.; Zhang, H. D.; He, W. Q.; Zhang, J. Q.; Daniel, D.; Yao, X. Directional pumping of water and oil microdroplets on slippery surface. *Proc. Natl. Acad. Sci. USA* **2019**, *116*, 2482–2487.

[9] Liu, M. J.; Wang, S. T.; Jiang, L. Nature-inspired superwettability systems. *Nat. Rev. Mater.* **2017**, *2*, 17036.

[10] Manna, U.; Lynn, D. M. Fabrication of liquid-infused surfaces using reactive polymer multilayers: Principles for manipulating the behaviors and mobilities of aqueous fluids on slippery liquid interfaces. *Adv. Mater.* **2015**, *27*, 3007–3012.

[11] Hou, X.; Zhang, Y. S.; Santiago, G. T. D.; Alvarez, M. M.; Ribas, J.; Jonas, S. J.; Weiss, P. S.; Andrews, A. M.; Aizenberg, J.; Khademhosseini, A. Interplay between materials and microfluidics. *Nat. Rev. Mater.* **2017**, *2*, 17016.

[12] Su, B.; Wang, S. T.; Song, Y. L.; Jiang, L. A miniature droplet reactor built on nanoparticle-derived superhydrophobic pedestals. *Nano Res.* **2010**, *4*, 266–273.

[13] Wei, Y. Y.; Cheng, G. Y.; Ho, H. P.; Ho, Y. P.; Yong, K. T. Thermodynamic perspectives on liquid-liquid droplet reactors for biochemical applications. *Chem. Soc. Rev.* **2020**, *49*, 6555–6567.

[14] Yao, Y. X.; Bennett, R. K. A.; Xu, Y.; Rather, A. M.; Li, S. C.; Cheung, T. C.; Bhanji, A.; Kreder, M. J.; Daniel, D.; Adera, S. et al. Wettability-based ultrasensitive detection of amphiphiles through directed concentration at disordered regions in self-assembled monolayers. *Proc. Natl. Acad. Sci. USA* **2022**, *119*, e2211042119.

[15] Li, W.; Tang, X.; Wang, L. Q. Photopyroelectric microfluidics. *Sci. Adv.* **2020**, *6*, eabc1693.

[16] Gao, Z. F.; Liu, R.; Wang, J. H.; Dai, J.; Huang, W. H.; Liu, M. J.; Wang, S. T.; Xia, F.; Jiang, L. Controlling droplet motion on an organogel surface by tuning the chain length of DNA and its biosensing application. *Chem* **2018**, *4*, 2929–2943.

[17] Courtney, M.; Chen, X. M.; Chan, S.; Mohamed, T.; Rao, P. P. N.; Ren, C. L. Droplet microfluidic system with on-demand trapping and releasing of droplet for drug screening applications. *Anal. Chem.* **2017**, *89*, 910–915.

[18] Li, A.; Li, H. Z.; Li, Z.; Zhao, Z. P.; Li, K. Z.; Li, M. Z.; Song, Y. L. Programmable droplet manipulation by a magnetic-actuated robot. *Sci. Adv.* **2020**, *6*, eaay5808.

[19] Wang, C.; Wang, D. Y.; Miao, W. N.; Shi, L. X.; Wang, S. T.; Tian, Y.; Jiang, L. Bioinspired ultrafast-responsive nanofluidic system for ion and molecule transport with speed control. *ACS Nano* **2020**, *14*, 12614–12620.

[20] Zhan, Y. Y.; Zhou, G. F.; Lamers, B. A. G.; Visschers, F. L. L.; Hendrix, M. M. R. M.; Broer, D. J.; Liu, D. Q. Artificial organic skin wets its surface by field-induced liquid secretion. *Matter* **2020**, *3*, 782–793.

[21] Zheng, Y. M.; Bai, H.; Huang, Z. B.; Tian, X. L.; Nie, F. Q.; Zhao, Y.; Zhai, J.; Jiang, L. Directional water collection on wetted spider silk. *Nature* **2010**, *463*, 640–643.

[22] Park, K. C.; Kim, P.; Grinthal, A.; He, N.; Fox, D.; Weaver, J. C.; Aizenberg, J. Condensation on slippery asymmetric bumps. *Nature* **2016**, *531*, 78–82.

[23] Ju, J.; Bai, H.; Zheng, Y. M.; Zhao, T. Y.; Fang, R. C.; Jiang, L. A multi-structural and multi-functional integrated fog collection system in cactus. *Nat. Commun.* **2012**, *3*, 1247.

[24] Tang, X.; Li, W.; Wang, L. Q. Furcated droplet motility on crystalline surfaces. *Nat. Nanotechnol.* **2021**, *16*, 1106–1112.

[25] Jin, Y. K.; Xu, W. H.; Zhang, H. H.; Li, R. R.; Sun, J.; Yang, S. Y.; Liu, M. J.; Mao, H. Y.; Wang, Z. K. Electrostatic tweezer for droplet manipulation. *Proc. Natl. Acad. Sci. USA* **2022**, *119*, e2105459119.

[26] Guo, T. Q.; Che, P. D.; Heng, L. P.; Fan, L. Z.; Jiang, L. Anisotropic slippery surfaces: Electric-driven smart control of a drop's slide. *Adv. Mater.* **2016**, *28*, 6999–7007.

[27] Zhang, P. R.; Chen, C. Y.; Su, X. Y.; Mai, J.; Gu, Y. Y.; Tian, Z. H.; Zhu, H. D.; Zhong, Z. W.; Fu, H.; Yang, S. J. et al. Acoustic streaming vortices enable contactless, digital control of droplets. *Sci. Adv.* **2020**, *6*, eaba0606.

[28] Collignon, S.; Friend, J.; Yeo, L. Planar microfluidic drop splitting and merging. *Lab Chip* **2015**, *15*, 1942–1951.

[29] Wang, F.; Liu, M. J.; Liu, C.; Zhao, Q. L.; Wang, T.; Wang, Z. K.; Du, Z. M. Light-induced charged slippery surfaces. *Sci. Adv.* **2022**, *8*, eabp9369.

[30] Tang, X.; Wang, L. Q. Loss-free photo-manipulation of droplets by pyroelectro-trapping on superhydrophobic surfaces. *ACS Nano* **2018**, *12*, 8994–9004.

[31] Timonen, J. V. I.; Latikka, M.; Leibler, L.; Ras, R. H. A.; Ikkala, O. Switchable static and dynamic self-assembly of magnetic droplets on superhydrophobic surfaces. *Science* **2013**, *341*, 253–257.

[32] Liu, X. B.; Kent, N.; Ceballos, A.; Streubel, R.; Jiang, Y. F.; Chai, Y.; Kim, P. Y.; Forth, J.; Hellman, F.; Shi, S. W. et al. Reconfigurable ferromagnetic liquid droplets. *Science* **2019**, *365*,

264–267.

[33] Zhang, J. Q.; Wang, X. J.; Wang, Z. Y.; Pan, S. F.; Yi, B.; Ai, L. Q.; Gao, J.; Mugele, F.; Yao, X. Wetting ridge assisted programmed magnetic actuation of droplets on ferrofluid-infused surface. *Nat. Commun.* **2021**, *12*, 7136.

[34] Feng, L.; He, X. Y.; Zhu, J. L.; Shi, W. Y. Magnetic manipulation of diamagnetic droplet on slippery liquid-infused porous surface. *Phys. Rev. Fluids* **2022**, *7*, 053602.

[35] Roy, P. K.; Bormashenko, E.; Frenkel, M.; Legchenkova, I.; Shoval, S. Magnetic field induced motion of water droplets and bubbles on the lubricant coated surface. *Colloid Surf. A* **2020**, *597*, 124773.

[36] Volk, A. A.; Epps, R. W.; Abolhasani, M. Accelerated development of colloidal nanomaterials enabled by modular microfluidic reactors: Toward autonomous robotic experimentation. *Adv. Mater.* **2021**, *33*, 2004495.

[37] Wang, W. D.; Timonen, J. V. I.; Carlson, A.; Drotlef, D. M.; Zhang, C. T.; Kolle, S.; Grinthal, A.; Wong, T. S.; Hatton, B.; Kang, S. H. et al. Multifunctional ferrofluid-infused surfaces with reconfigurable multiscale topography. *Nature* **2018**, *559*, 77–82.

[38] Guo, P.; Wang, Z. B.; Heng, L. P.; Zhang, Y. Q.; Wang, X.; Jiang, L. Magnetocontrollable droplet and bubble manipulation on a stable amphibious slippery gel surface. *Adv. Funct. Mater.* **2019**, *29*, 1808717.

[39] Lou, X. D.; Huang, Y.; Yang, X.; Zhu, H.; Heng, L. P.; Xia, F. External stimuli responsive liquid-infused surfaces switching between slippery and nonslippery states: Fabrications and applications. *Adv. Funct. Mater.* **2020**, *30*, 1901130.

[40] Demus, D.; Goodby, J.; Gray, G. W.; Spiess, H. W.; Vill, V. *Handbook of Liquid Crystals*: *Low Molecular Weight Liquid Crystals I*; Wiley-VCH Verlag GmbH: New York, 1998.

[41] Schadt, M. Liquid crystal materials and liquid crystal displays. *Annu. Rev. Mater. Sci.* **1997**, *27*, 305–379.

[42] Bukusoglu, E.; Pantoja, M. B.; Mushenheim, P. C.; Wang, X. G.; Abbott, N. L. Design of responsive and active (soft) materials using liquid crystals. *Annu. Rev. Chem. Biomol. Eng.* **2016**, *7*, 163–196.

[43] Kim, Y. K.; Wang, X. G.; Mondkar, P.; Bukusoglu, E.; Abbott, N. L. Self-reporting and self-regulating liquid crystals. *Nature* **2018**, *557*, 539–544.

[44] Kim, I.; Ansari, M. A.; Mehmood, M. Q.; Kim, W. S.; Jang, J.; Zubair, M.; Kim, Y. K.; Rho, J. Stimuli-responsive dynamic metaholographic displays with designer liquid crystal modulators. *Adv. Mater.* **2020**, *32*, 2004664.

[45] Turiv, T.; Koizumi, R.; Thijssen, K.; Genkin, M. M.; Yu, H.; Peng, C. H.; Wei, Q. H.; Yeomans, J. M.; Aranson, I. S.; Doostmohammadi, A. et al. Polar jets of swimming bacteria condensed by a patterned liquid crystal. *Nat. Phys.* **2020**, *16*, 481–487.

[46] Xu, Y.; Rather, A. M.; Song, S.; Fang, J. C.; Dupont, R. L.; Kara, U. I.; Chang, Y.; Paulson, J. A.; Qin, R. J.; Bao, X. P. et al. Ultrasensitive and selective detection of SARS-CoV-2 using thermotropic liquid crystals and image-based machine learning. *Cell Rep. Phys. Sci.* **2020**, *1*, 100276.

[47] Kléman, M.; Lavrentovich, O. D. *Soft Matter Physics*: *An Introduction*; Springer: New York, 2003,

[48] Turiv, T.; Lazo, I.; Brodin, A.; Lev, B. I.; Reiffenrath, V.; Nazarenko, V. G.; Lavrentovich, O. D. Effect of collective molecular reorientations on brownian motion of colloids in nematic liquid crystal. *Science* **2013**, *342*, 1351–1354.

[49] Xu, Y.; Rather, A. M.; Yao, Y. X.; Fang, J. C.; Mamtani, R. S.; Bennett, R. K. A.; Atta, R. G.; Adera, S.; Tkalec, U.; Wang, X. G. Liquid crystal-based open surface microfluidics manipulate liquid mobility and chemical composition on demand. *Sci. Adv.* **2021**, *7*, eabi7607.

[50] Xu, Y.; Chang, Y.; Yao, Y. X.; Zhang, M.; Dupont, R. L.; Rather, A. M.; Bao, X. P.; Wang, X. G. Modularizable liquid-crystal-based open surfaces enable programmable chemical transport and feeding using liquid droplets. *Adv. Mater.* **2022**, *34*, 2108788.

[51] K&J Magnetics, Inc [Online]. https://www.kjmagnetics.com/. (Accessed on Oct 29, 2022).

[52] Gim, M. J.; Beller, D. A.; Yoon, D. K. Morphogenesis of liquid crystal topological defects during the nematic-smectic a phase transition. *Nat. Commun.* **2017**, *8*, 15453.

[53] Honglawan, A.; Beller, D. A.; Cavallaro, M. Jr.; Kamien, R. D.; Stebe, K. J.; Yang, S. Topographically induced hierarchical assembly and geometrical transformation of focal conic domain arrays in smectic liquid crystals. *Proc. Natl. Acad. Sci. USA* **2013**, *110*, 34–39.

[54] Yoon, D. K.; Deb, R.; Chen, D.; Körblova, E.; Shao, R. F.; Ishikawa, K.; Rao, N. V. S.; Walba, D. M.; Smalyukh, I. I.; Clark, N. A. Organization of the polarization splay modulated smectic liquid crystal phase by topographic confinement. *Proc. Natl. Acad. Sci. USA* **2010**, *107*, 21311–21315.

[55] Zappone, B.; Meyer, C.; Bruno, L.; Lacaze, E. Periodic lattices of frustrated focal conic defect domains in smectic liquid crystal films. *Soft Matter* **2012**, *8*, 4318–4326.

[56] Rather, A. M.; Xu, Y.; Chang, Y.; Dupont, R. L.; Borbora, A.; Kara, U. I.; Fang, J. C.; Mamtani, R.; Zhang, M.; Yao, Y. X. et al. Stimuli-responsive liquid-crystal-infused porous surfaces for manipulation of underwater gas bubble transport and adhesion. *Adv. Mater.* **2022**, *34*, 2110085.

[57] Gao, N.; Geyer, F.; Pilat, D. W.; Wooh, S.; Vollmer, D.; Butt, H. J.; Berger, R. How drops start sliding over solid surfaces. *Nat. Phys.* **2018**, *14*, 191–196.

[58] Mirsaidov, U. M.; Zheng, H. M.; Bhattacharya, D.; Casana, Y.; Matsudaira, P. Direct observation of stick-slip movements of water nanodroplets induced by an electron beam. *Proc. Natl. Acad. Sci. USA* **2012**, *109*, 7187–7190.

[59] Sun, L. Y.; Bian, F. K.; Wang, Y.; Wang, Y. T.; Zhang, X. X.; Zhao, Y. J. Bioinspired programmable wettability arrays for droplets manipulation. *Proc. Natl. Acad. Sci. USA* **2020**, *117*, 4527–4532.

[60] Wang, B. L.; Heng, L. P.; Jiang, L. Temperature-responsive anisotropic slippery surface for smart control of the droplet motion. *ACS Appl. Mater. Interfaces* **2018**, *10*, 7442–7450.

[61] Kreder, M. J.; Daniel, D.; Tetreault, A.; Cao, Z. L.; Lemaire, B.; Timonen, J. V. I.; Aizenberg, J. Film dynamics and lubricant depletion by droplets moving on lubricated surfaces. *Phys. Rev. X* **2018**, *8*, 031053.

[62] Daniel, D.; Timonen, J. V. I.; Li, R. P.; Velling, S. J.; Aizenberg, J. Oleoplaning droplets on lubricated surfaces. *Nat. Phys.* **2017**, *13*, 1020–1025.

[63] Smith, J. D.; Dhiman, R.; Anand, S.; Reza-Garduno, E.; Cohen, R. E.; McKinley, G. H.; Varanasi, K. K. Droplet mobility on lubricant-impregnated surfaces. *Soft Matter* **2013**, *9*, 1772–1780.

[64] Xu, W.; Choi, C. H. From sticky to slippery droplets: Dynamics of contact line depinning on superhydrophobic surfaces. *Phys. Rev. Lett.* **2012**, *109*, 024504.

[65] Malinowski, R.; Parkin, I. P.; Volpe, G. Advances towards programmable droplet transport on solid surfaces and its applications. *Chem. Soc. Rev.* **2020**, *49*, 7879–7892.

[66] Gao, L. C.; McCarthy, T. J. Contact angle hysteresis explained. *Langmuir* **2006**, *22*, 6234–6237.

[67] De Gennes, P. G.; Brochard-Wyart, F.; Quéré, D. *Capillarity and Wetting Phenomena Drops*, *Bubbles*, *Pearls*, *Waves*; Springer: New York, 2004.

[68] Daniel, D.; Timonen, J. V. I.; Li, R. P.; Velling, S. J.; Kreder, M. J.; Tetreault, A.; Aizenberg, J. Origins of extreme liquid repellency on structured, flat, and lubricated hydrophobic surfaces. *Phys. Rev. Lett.* **2018**, *120*, 244503.

[69] Landau, L. ; Levich, B. Dragging of a liquid by a moving plate. In *Dynamics of Curved Fronts*. Pelcé, P., Ed.; Academic Press: Boston, 1988, 141–153.

[70] Wong, T. S.; Kang, S. H.; Tang, S. K. Y.; Smythe, E. J.; Hatton, B. D.; Grinthal, A.; Aizenberg, J. Bioinspired self-repairing slippery surfaces with pressure-stable omniphobicity. *Nature* **2011**, *477*, 443–447.

[71] De Gennes, P. G.; Prost, J. *The Physics of Liquid Crystals*;

Clarendon Press; Oxford University Press: Oxford, 1993.

[72] Chmielewski, A. G. Viscosity coefficients of some nematic liquid crystals. *Mol. Cryst. Liq. Cryst.* **1986**, *132*, 339–352.

[73] Mottram, N. J.; Hogan, S. J. Magnetic field-induced changes in molecular order in nematic liquid crystals. *Continuum Mech. Thermodyn.* **2002**, *14*, 281–295.

[74] Concellón, A.; Zentner, C. A.; Swager, T. M. Dynamic complex liquid crystal emulsions. *J. Am. Chem. Soc.* **2019**, *141*, 18246–18255.

[75] Kikuchi, H. Liquid crystalline blue phases. In *Liquid Crystalline Functional Assemblies and Their Supramolecular Structures*. Kato, T., Ed.; Springer: Berlin, 2008; pp 99–117.

[76] Martínez-González, J. A.; Zhou, Y.; Rahimi, M.; Bukusoglu, E.; Abbott, N. L.; De Pablo, J. J. Blue-phase liquid crystal droplets. *Proc. Natl. Acad. Sci. USA* **2015**, *112*, 13195–13200.

[77] Borshch, V.; Kim, Y. K.; Xiang, J.; Gao, M.; Jákli, A.; Panov, V. P.; Vij, J. K.; Imrie, C. T.; Tamba, M. G.; Mehl, G. H. et al. Nematic twist-bend phase with nanoscale modulation of molecular orientation. *Nat. Commun.* **2013**, *4*, 2635.

[78] Chen, D.; Porada, J. H.; Hooper, J. B.; Klittnick, A.; Shen, Y. Q.; Tuchband, M. R.; Korblova, E.; Bedrov, D.; Walba, D. M.; Glaser, M. A. et al. Chiral heliconical ground state of nanoscale pitch in a nematic liquid crystal of achiral molecular dimers. *Proc. Natl. Acad. Sci. USA* **2013**, *110*, 15931–15936.

[79] Lee, C.; Kim, H.; Nam, Y. Drop impact dynamics on oil-infused nanostructured surfaces. *Langmuir* **2014**, *30*, 8400–8407.